

1 **Synthesis of Fe_3O_4 / ZnO/CuO Nanocomposite and its Sono-**
2 **photocatalyst property for removal of methylene blue from**
3 **wastewater**

4
5 **Samira Pishkar Ahrab¹, Mahdiyeh pourali², MohammadTaghi Hamedani^{*1},**

6
7 1. Faculty of Mechanical Engineering, Tabriz University, Tabriz, 51616471, Iran.
8 2. Faculty of Materials Engineering, Sahand University of Technology, Tabriz, 513351996, Iran.
9

10 **Abstract**

11 $\text{Fe}_3\text{O}_4/\text{ZnO}/\text{CuO}$ nanocomposites with various molar ratios of CuO were successfully synthesized. Sol-
12 gel method was used to synthesize nanocomposite materials at a low temperature. A set of experiments,
13 including X-ray diffraction (XRD), Dynamic Light Scattering (DLS), scanning electron microscopy
14 (SEM), and UV-Vis spectroscopy, was used to confirm the successful synthesis of $\text{Fe}_3\text{O}_4/\text{ZnO}/\text{CuO}$
15 nanocomposites in crystalline form.

16 The photocatalytic activity of the samples was investigated via the degradation of methylene blue (MB)
17 dye from synthetic wastewater under three distinct conditions: visible light, ultraviolet light, and a
18 combination of visible light with ultrasonic treatment. $\text{Fe}_3\text{O}_4/\text{ZnO}/\text{CuO}$ nanocomposite with a molar ratio
19 of 1:1:0.5 showed the highest photocatalytic activity when irradiated with either visible or ultraviolet light.
20 Furthermore, when visible light was combined with ultrasonic treatment, complete (100%) removal of
21 methylene blue was achieved within 120 minutes. The results demonstrate that these nanocomposites are
22 efficient catalysts for wastewater treatment through the removal of organic pollutants.
23

24 **Keywords** $\text{Fe}_3\text{O}_4/\text{ZnO}/\text{CuO}$, Sono-photocatalyst, nanocomposite, Wastewater treatment
25
26

27 **1 Introduction**

28 Over the past few decades, there have been
29 some emerging problems in the industry,
30 whereas environmental pollution has attracted
31 a lot of attention in the world [1]. The release
32 of organic dyes from the textile, leather, food,
33 cosmetics, and pharmaceutical industries into
34 the environment has resulted in significant
35 issues for living organisms. Also, water
36 pollution is a problem that should be identified
37 as soon as possible. Researchers have done a
38 great deal of research on how to treat infected
39 water from the processing of industrial
40 products and household waste [2].

41 Nevertheless, the conventional wastewater
42 treatment method still contains a large number
43 of contaminants that are challenging to
44 eliminate. For instance, antibiotics, dyes,
45 organic insecticides, multi-rheological
46 aromatic hydrocarbons [3-6], etc. New
47 techniques, like Fenton oxidation [7] and a
48 hybrid approach that combines multiple
49 purification processes, like active carbon,
50 biofilm, enzymatic reactors, etc., have been
51 developed to remove these contaminants [8].
52 These techniques have garnered interest from
53 researchers [9] and have a positive impact on
54 the degradation of contaminated organic
55 matter. Another method for removing

* Corresponding author

Professor of Materials science and engineering, Mechanic faculty, Tabriz university, Tabriz ,Iran.

Email m.hamedani.tabrizu@gmail.com, Tel: +989147618082 & +98-41-33356026, Fax: +98-41-33354153

56 pollutants is to use Semiconducting oxides with
57 photocatalytic properties. Various catalysts
58 have been introduced to remove pollutants or
59 even make them non-irritating chemicals [10].
60 Among them, TiO_2 and ZnO semiconductors
61 have been introduced as successful
62 photocatalysts for the destruction of organic
63 pollutants. The advantages of ZnO
64 nanoparticles include strong oxidizing ability,
65 light sensitivity, excellent mechanical and
66 chemical stability, non-toxic nature, favorable
67 energy gap, and cheap price [11]. However, to
68 use ZnO as a photocatalyst, according to the
69 band gap (3.2 electron volts), it is necessary to
70 use ultraviolet light that only contains less than
71 10% of the sun's light. While in the sunlight,
72 45% of the radiation is visible in the lightrange
73 [12,13]. To enhance the photocatalytic activity
74 of ZnO under the influence of visible light,
75 solutions need to be considered. The formation
76 of a ZnO nanoparticle composite with other
77 metal oxides results in the absorption of
78 stronger light and increased ability to absorb
79 visible light [14]. In addition, this composite
80 prevents recombining electron-hole and
81 increases the photocatalyst's efficiency [15].
82 The coupling of ZnO with CuO nanoparticles
83 and their composite formation is a promising
84 method for increasing photocatalytic
85 properties. Besides extending the absorption
86 range towards the visible light, this method
87 transmits electrons produced by the photon
88 from a high-conductivity band of CuO to a low-
89 conductivity band of ZnO , which results in the
90 effective separation of the electron-hole [16].
91 So far, considerable research has been done on
92 the synthesis of ZnO / CuO as a special high-
93 level catalyst. Number of techniques have been
94 put up to create a ZnO/CuO catalyst, such as
95 mechanical methods, for example grinding wet
96 chemistry, coprecipitation, thermal
97 decomposition, sol-gel, hydrothermal, and
98 photo deposition methods [17]. Another
99 problem for catalysts is their segregation from
100 purified water in practical applications.
101 Traditional methods such as coagulation and
102 filtration cause catalyst degradation and
103 increase energy consumption [18]. Using an
104 external magnet, researchers have recently
105 paired magnetic nanoparticles with

106 photocatalytically active materials to improve
107 catalyst separation and recycling [19].
108 Therefore, the introduction of magnetic
109 materials such as Fe_3O_4 in $\text{Fe}_3\text{O}_4/\text{ZnO}/\text{CuO}$
110 nanocomposites simplifies the magnetic
111 separation. Nanocatalysts are beneficial for
112 academic and industrial research due to their
113 high reaction rates, perfect activation of
114 adsorbed compounds, ease of use, high
115 selectivity, recyclability, and eco-friendliness.
116 Because of their appealing features, nanometal
117 oxides have been utilized as solid catalysts in a
118 variety of organic processes [20].
119 In explaining the photocatalytic effect, it can be
120 said that in the absence of degradation matter,
121 hydrocarbons often decompose slowly.
122 Photocatalyst reduces the activation energy of
123 the decomposition process and therefore,
124 accelerates the reaction. As a result of the light
125 collision with photocatalytic materials,
126 electron holes create high oxidation and
127 resuscitation [21].
128 Nowadays, the use of ultrasonics in the
129 presence of a catalyst (sonocatalytic
130 decomposition) is an eco-friendly method for
131 removing dyes from wastewater. The influence
132 of ultrasonic waves is the heat produced by a
133 hole explosion, which converts water
134 molecules into hydroxyl radicals and reactive
135 hydrogen atoms. Both species can react with
136 organic dyes, which can lead to the breakdown
137 and elimination of different contaminants from
138 wastewater[22].
139 As a result, the simultaneous use of light and
140 ultrasonic radiation to analyze different colors
141 has been investigated [19-22].
142 In the current study, the impact of light and
143 ultrasound irradiation and the metal oxide
144 content has been investigated on the
145 photocatalytic activity of the $\text{Fe}_3\text{O}_4/\text{ZnO}/\text{CuO}$
146 nanocomposites. The optical and
147 morphological analysis proceeded with a
148 photocatalytic activity test in methylene blue
149 (MB) degradation from wastewater.
150

151 **2 EXPERIMENTAL PROCEDURES**

152

153 In this study Iron (II) sulfate heptahydrate
154 ($\text{FeSO}_4 \cdot 7\text{H}_2\text{O}$, 99%), copper sulfate
155 pentahydrate ($\text{CuSO}_4 \cdot 5\text{H}_2\text{O}$, 99%), zinc sulfate

156 heptahydrate ($\text{ZnSO}_4 \cdot 7\text{H}_2\text{O}$, 99%) and sodium
157 hydroxide (NaOH) (Merck Company) was
158 used as raw materials.

159 CuO and Fe_3O_4 nanoparticles were synthesized
160 using the sol-gel method. In this method, 0.025
161 mole of $\text{CuSO}_4 \cdot 5\text{H}_2\text{O}$ was dissolved in 100 mL
162 of deionized water with constant magnetic
163 stirring. Then 0.05 mole of NaOH was
164 dissolved in 150 mL of deionized water and
165 added to the solution in a droplet form to obtain
166 the appropriate pH. The solution was then
167 maintained at 80°C for 3 hours to form the gel.
168 After 4 hours, the black product was dissolved
169 using filter paper and dried at 80°C for 4 hours
170 in an oven to achieve Copper oxide
171 nanoparticles.

172 To obtain Fe_3O_4 nanoparticles, 0.027 mole of
173 $\text{FeSO}_4 \cdot 7\text{H}_2\text{O}$, dissolved in 100 mL of deionized
174 water and continuously stirred at room
175 temperature. To control the pH in 3, acetic acid
176 (CH_3COOH) and 30 mL of ethylene glycol
177 (EG), both of them in pure form, were added to
178 the solution. Then, 0.054 mole of NaOH was
179 dissolved in 150 mL of deionized water and
180 added dropwise to the mixture. The final
181 solution was stirred at 80°C for 3 h to form a
182 gel. The gel was dried at 80°C for 4 h.
183 To synthesize the $\text{Fe}_3\text{O}_4/\text{ZnO}/\text{CuO}$
184 nanocomposite, 0.0125 mole of $\text{ZnSO}_4 \cdot 7\text{H}_2\text{O}$
185 was dissolved in 30 mL of distilled water with
186 magnetic stirring. Then, 0.025 mole of NaOH
187 in 65 mL of deionized water was added to the
188 solution in droplets to reach the appropriate
189 PH, which was then stirred and heated at 80°C .
190 The previously synthesized Fe_3O_4 and CuO
191 nanoparticles were dispersed in 30 mL of
192 ethanol (99.7%) and then added to the initial
193 solution. The resulting mixture was
194 continuously stirred at 80°C for 2 hours.
195 Finally, ZnO was formed in situ on the surface
196 of the pre-formed Fe_3O_4 and CuO . At the end
197 the product was isolated using filter paper and
198 washed several times with distilled water and
199 ethanol to remove impurities. The final product
200 was left at room temperature overnight and
201 dried at 100°C for 1 hour. Nanocomposite
202 $\text{Fe}_3\text{O}_4/\text{ZnO}/\text{CuO}$ with the molar ratios of
203 (1:1:0.3, 1:1:0.5, 1:1:1, 1:1:3) was prepared by
204 changing the concentrations of the precursor
205 solutions and evaluated.

206 X-ray diffraction peaks were measured by an
207 XRD analyzer (Siemens D5000 X-ray
208 diffractometer). The analysis was conducted
209 under the conditions of $\text{Cu-}\kappa\alpha$ radiation
210 ($\lambda=1.54178\text{\AA}$), a scanning rate of $20^\circ/\text{min}$, a 20
211 range of 20 – 80° , and operating conditions of 30
212 kV and 40 mA. Also, Crystallite size is
213 estimated by Scherer's equation (Eq.1) [23]:
214 $D=0.9\lambda/\beta\cos\Theta$ (Eq. 1)

215 where D is the size of the crystals in
216 nanometers, β is the peak width at half the
217 maximum intensity in radians in radian, λ is the
218 x-ray wavelength in nanometers, and Θ is the
219 Bragg angle corresponding to the diffraction
220 peak.

221 SEM (Stereo Scan 360) was conducted to
222 verify the morphology of the obtained
223 nanoparticles. Elemental analysis of the
224 samples was performed using X-ray diffraction
225 spectroscopy (EDX). A dot map was used to
226 determine the distribution of the elements in the
227 nanocomposite. To investigate particle size
228 distribution from DLS, Nanotrac Wave of
229 Micro trac Co. was used and to determine the
230 adsorption edge and band gap of synthesized
231 zinc oxide and prepared nanocomposites, DRS
232 spectroscopic analysis was performed. The
233 absorption wavelength was obtained by
234 extrapolating the linear part of the absorption
235 intensity curve in terms of wavelength.

236 Eq. 2 was used to calculate the band gap [24]:
237 $Eg = hc / \lambda g$ (Eq. 2)

238 In this respect, Eg is the band gap in electron
239 volts, h is the Planck constant equals
240 4.13567×10^{-15} ev, c is the light speed equals
241 299792458 m / s and λg is the absorption
242 wavelength.

243 The effectiveness of the photocatalysts was
244 tested by measuring their ability to break down
245 methylene blue (MB) in 100 mL beakers. In
246 this test, the UV-C Philips 9W lamp was used
247 as UV light and the 120-watt metal halide lamp
248 was used as a visible light source. A
249 photocatalytic test equipment was mounted and
250 sealed in a dark chamber to prevent the loss of
251 radiation. For the determination of
252 photocatalytic activity, 0.05 g of the
253 nanocomposite samples was dispersed in 100
254 ml of MB solution with a concentration of
255 0.005 g / l using a magnetic stirrer.
256 Before illumination, the reaction mixture was

257 kept in dark conditions for 20 minutes to
 258 establish adsorption-desorption equilibrium.
 259 After collecting the initial sample, the
 260 photocatalytic reaction was initiated by
 261 activating the light source. Subsequent samples
 262 were collected at 20-minute intervals
 263 (specifically at 20, 40, 60, 80, 100, and 120
 264 minutes), and each sample underwent UV-Vis
 265 spectroscopic analysis. The concentration of
 266 Methylene Blue (MB) was determined by
 267 measuring the UV-Vis absorbance at its
 268 characteristic peak wavelength of 665 nm. A
 269 calibration curve was created and used to
 270 convert the measured absorbance values into
 271 actual dye concentrations. The degradation rate
 272 was then determined using the following
 273 equation [25]:
 274

$$275 \quad (I_0 - I_t)/I_0 \times 100 = (C_0 - C_t)/C_0 \times 100 \quad (\text{Eq. 3})$$

276
 277 Where C represents the concentration of
 278 Methylene Blue (MB) at any given time during
 279 the reaction, while C₀ is the initial MB
 280 concentration after reaching adsorption-
 281 desorption equilibrium, similarly, A represents
 282 the absorbance value measured at any point
 283 during the reaction, and A₀ is the initial
 284 absorbance value recorded at equilibrium.
 285 To evaluate how ultrasonic treatment affects
 286 photocatalytic activity, Fe₃O₄/ZnO/CuO
 287 nanocomposites (0.05 g) with varying molar
 288 ratios were dispersed in Methylene Blue
 289 solution (100 mL, 0.005 g/L) using
 290 ultrasonication and subjected to visible light
 291 irradiation for intervals of 20, 40, 60, 80, 100
 292 and 120 minutes.
 293

294 3 Results and Discussions

295
 296 The XRD patterns shown in Fig. 1 display the
 297 diffraction patterns of Fe₃O₄/ZnO/CuO
 298 nanocomposites that were synthesized in
 299 different molar ratios of CuO. The patterns
 300 exhibit characteristic diffraction peaks
 301 corresponding to cubic spinel Fe₃O₄,
 302 monoclinic CuO, and hexagonal wurtzite ZnO
 303 structures. The absence of any impurities or
 304 secondary phases in the patterns demonstrates
 305 that the Fe₃O₄/ZnO/CuO nanocomposites were
 306 synthesized successfully. All XRD peaks
 307 corresponding to [101] Planes related to

308 hexagonal ZnO structure (2 Θ =32.5), [200]
 309 planes related to CuO monoclinic structure (2 Θ
 310 =39.5) and [311] planes for cubic spinel
 311 structure Fe₃O₄ (2 Θ =35.5) have the highest
 312 growth rates. Furthermore, analysis of the XRD
 313 patterns for Fe₃O₄/ZnO/CuO nanocomposites
 314 with varying molar ratios reveals a clear trend:
 315 as the molar ratio of CuO to ZnO increases,
 316 there is a corresponding increase in the
 317 intensity of CuO diffraction peaks, while
 318 simultaneously showing a decrease in the
 319 intensity of both ZnO and Fe₃O₄ diffraction
 320 peaks. Changes in the intensity of the pattern
 321 revealed the increase of CuO content within
 322 the nanocomposite structure.

323 In all XRD diagrams, considering the peak
 324 positions, it can be seen that ZnO does not form
 325 a solid solution with CuO and Fe₃O₄, and the
 326 Fe₃O₄/ZnO/CuO nanocomposite is considered
 327 as a nanocomposite powder of ZnO, Fe₃O₄ and
 328 CuO crystals.

329 Fig. 2 shows the XRD pattern of
 330 Fe₃O₄/ZnO/CuO nanocomposite with molar
 331 ratios of 1:1:0.3, 1:1:0.5, 1:1:1, and 1:1:3 for
 332 a,b,c, and d images, respectively. According to
 333 reference data, 01-075-0033 demonstrated
 334 Fe₃O₄ in the cubic phase, 0254-041-00
 335 determined the hexagonal crystalline phase of
 336 ZnO, and 0704-076-01 demonstrated CuO with
 337 a monoclinic crystalline structure.

338 In Table. 1, the particle size of Fe₃O₄, ZnO,
 339 CuO, and Fe₃O₄/ZnO/CuO nanocomposites
 340 with molar ratios of 1:1:0.3, 1:1:0.5, 1:1:1 and
 341 1:1:3 estimated by Scherrer's equation. By
 342 comparing the size of Fe₃O₄, ZnO, and CuO
 343 particles in Fe₃O₄/ZnO/CuO nanocomposites
 344 with different molar ratios, it is observed that
 345 the presence of CuO inhibits the growth of
 346 particles and reduces the size of ZnO and Fe₃O₄
 347 particles. In conclusion, CuO nanoparticles
 348 inhibit the growth of ZnO crystallites. It was
 349 evidenced by the significant reduction in ZnO
 350 crystallite size in the presence of CuO. In
 351 contrast, Fe₃O₄ crystallite size shows a smaller

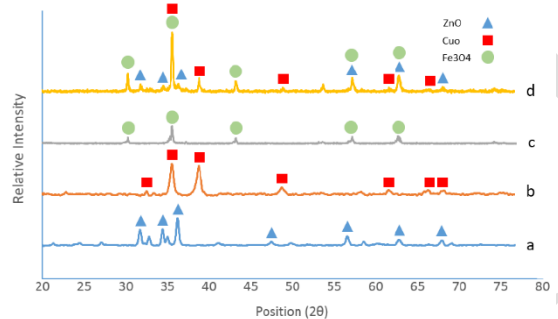
352 decrease, indicating that CuO has a less
 353 pronounced effect on the growth of Fe_3O_4
 354 crystallites. The crystallite size of CuO varies
 355 depending on its concentration in the
 356 composites, highlighting its role in controlling
 357 crystallite growth in nanocomposites.

358 **Table1.** crystallite size of ZnO, CuO, and Fe_3O_4 in
 359 $\text{Fe}_3\text{O}_4/\text{ZnO}/\text{CuO}$ nanocomposite

| samples | ZnO crystallite size (nm) | CuO crystallite size (nm) | Fe_3O_4 crystallite size (nm) |
|--|---------------------------|---------------------------|---|
| Fe_3O_4 | - | - | 44.5 |
| CuO | - | 19.31 | - |
| ZnO | 22.92 | - | - |
| $\text{Fe}_3\text{O}_4/\text{ZnO}/\text{CuO}(1:1:0.3)$ | 19.21 | 20.15 | 44.01 |
| $\text{Fe}_3\text{O}_4/\text{ZnO}/\text{CuO}(1:1:0.5)$ | 20.18 | 16.15 | 42.23 |
| $\text{Fe}_3\text{O}_4/\text{ZnO}/\text{CuO}(1:1:1)$ | 19.65 | 18.62 | 41.15 |
| $\text{Fe}_3\text{O}_4/\text{ZnO}/\text{CuO}(1:1:3)$ | 17.15 | 21.48 | 40.15 |

3

361



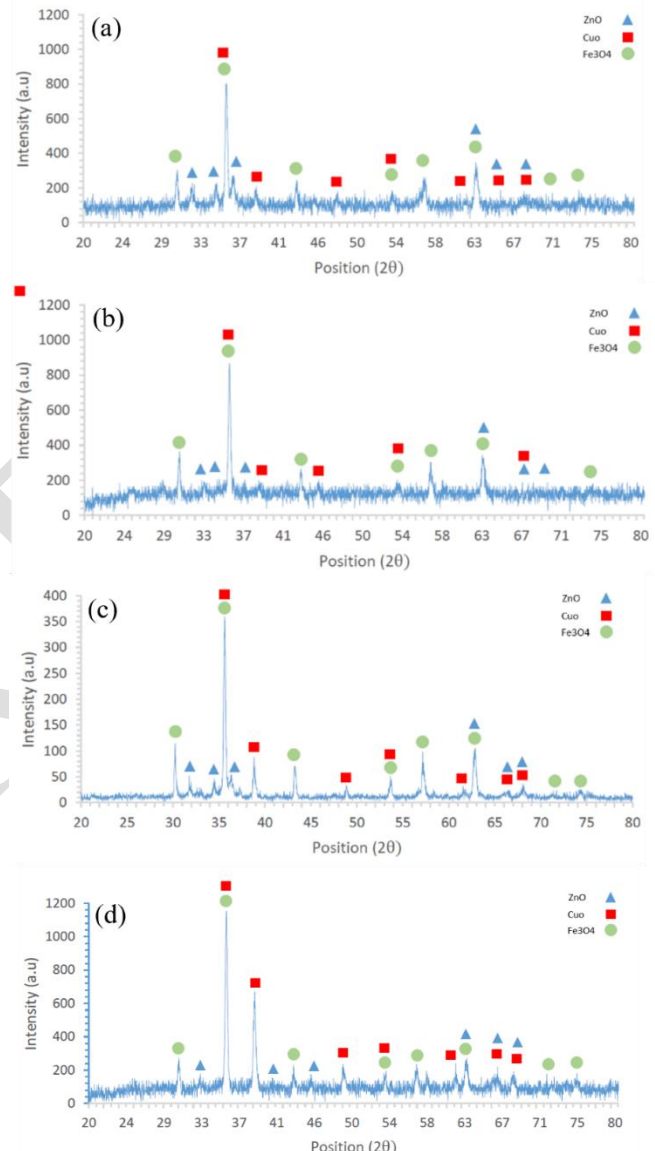
362

363 **Fig. 1.** XRD patterns of synthesized
 364 $\text{Fe}_3\text{O}_4/\text{ZnO}/\text{CuO}$ nanocomposite: (a) ZnO, (b)
 365 CuO, (c) Fe_3O_4 , (d) $\text{Fe}_3\text{O}_4/\text{ZnO}/\text{CuO}$
 366 nanocomposite.

367 Particle morphology of nanocomposites was
 368 investigated by scanning electron microscopy
 369 (SEM). Fig. 3 illustrates an SEM image of a
 370 $\text{Fe}_3\text{O}_4/\text{ZnO}/\text{CuO}$ nanocomposite with a molar
 371 ratio of 1:1:0.5. As shown in Fig.3, the
 372 $\text{Fe}_3\text{O}_4/\text{ZnO}/\text{CuO}$ nanocomposite is
 373 cauliflower-shaped. To compare the results, the
 374 size distribution of the conventional and
 375 synthesized catalysts was considered using
 376 ImageJ software. The analysis revealed that the
 377 synthesized samples exhibited relatively small
 378 average particle dimensions. This size
 379 distribution indicates the successful formation

381 of nanostructured materials. Similar
 382 $\text{Fe}_3\text{O}_4/\text{ZnO}/\text{CuO}$ morphologies have been
 383 reported in previous studies[20].

384



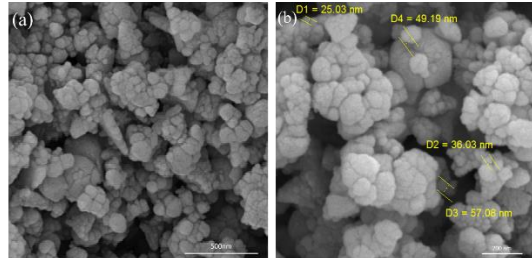
385
 386 **Fig. 2.** XRD patterns of synthesized
 387 $\text{Fe}_3\text{O}_4/\text{ZnO}/\text{CuO}$ nanocomposite: (a)
 388 $\text{Fe}_3\text{O}_4/\text{ZnO}/\text{CuO}(1:1:0.3)$,
 389 (b) $\text{Fe}_3\text{O}_4/\text{ZnO}/\text{CuO}(1:1:0.5)$, (c) $\text{Fe}_3\text{O}_4/\text{ZnO}/\text{CuO}$
 390 (1:1:1) and (d) $\text{Fe}_3\text{O}_4/\text{ZnO}/\text{CuO}(1:1:3)$.

391

392 Above all, the numerous pores of different
 393 sizes within the 3D microstructure act as
 394 transport pathways for small molecules. This
 395 morphology and porosity provide a larger
 396 surface area for dye adsorption and catalytic
 397 reactions. The reduction in particle dimensions

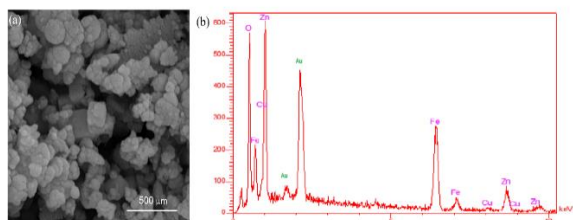
398 enhances the generation of electron-hole pairs
399 when exposed to light, resulting in more
400 effective degradation of contaminants during
401 performance testing.

402



403
404 **Fig. 3.** SEM image of synthesized $\text{Fe}_3\text{O}_4/\text{ZnO}/\text{CuO}$
405 nanocomposite, (a)SEM Mag 70kx
406 (b) SEM Mag 100kx Particle Size Distribution
407

408 EDX analysis aims to define the dispersion of
409 the elements on the surface of the catalyst. As
410 shown in Fig. 4, the characteristic peaks of the
411 elements of oxygen, iron, copper, and zinc
412 indicate the presence of these elements in the
413 nanocomposite structure. It should be noted
414 that the samples had no impurities. The peak in
415 the range of 1.8 and 2.2 keV is related to the
416 gold element, covered on the nanocomposite in
417 SEM analysis, to provide conductivity in the
418 sample. Also in Table 2, the weight percentage
419 and atomic percentage of the elements are
420 specified, which proves the proper synthesis of
421 the samples.



422
423 **Fig. 4.** EDX analysis of synthesized
424 $\text{Fe}_3\text{O}_4/\text{ZnO}/\text{CuO}$ nanocomposite: (a) SEM image
425 of the area selected for EDX analysis, (b) EDX
426 results in $\text{Fe}_3\text{O}_4/\text{ZnO}/\text{CuO}$ nanocomposite (1:1:0.5)

427

428

429

430

431 **Table 2.** Comparative amount of elements in the
432 structure of $\text{Fe}_3\text{O}_4/\text{ZnO}/\text{CuO}$ nanocomposite
(1:1:0.5)

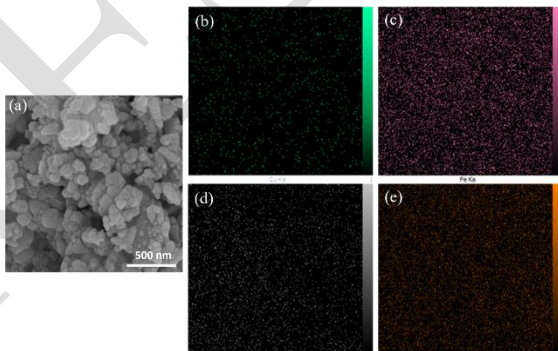
433

434

| samples | Weight percentage (% W) | Atomic percentage (% A) |
|------------------------------|-------------------------|-------------------------|
| $\text{O}_{\text{K}\alpha}$ | 28.77 | 60.03 |
| $\text{Cu}_{\text{K}\alpha}$ | 1.72 | 0.9 |
| $\text{Zn}_{\text{K}\alpha}$ | 28.38 | 14.49 |
| $\text{Fe}_{\text{K}\alpha}$ | 41.12 | 24.57 |

435

436 To investigate the distribution of elements in
437 the photocatalyst structure, dot Map analysis
438 was prepared from $\text{Fe}_3\text{O}_4/\text{ZnO}/\text{CuO}$
439 nanocomposite (1:1:0.5) as shown in Fig. 5.
440 The elemental distribution analysis of the
441 photocatalyst structure was conducted on the
442 selected region shown in Fig. 5a. Images 5b,
443 5c, 5d, and 5e show the distribution of copper,
444 iron, zinc, and oxygen, respectively. Moreover,
445 the elements are homogeneously distributed in
446 the structure.



477
478 **Fig. 5.** Dot map analysis of synthesized
479 $\text{Fe}_3\text{O}_4/\text{ZnO}/\text{CuO}$ nanocomposite: (a) Selected area
480 for dot map analysis, (b) Cu, (c) Fe, (d) Zn, (e) O

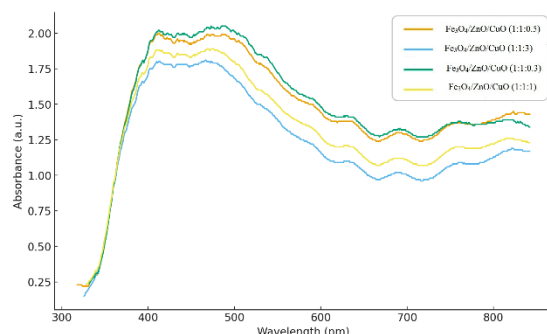
481

482 In this study, the photocatalytic performance of
483 $\text{Fe}_3\text{O}_4/\text{ZnO}/\text{CuO}$ nanocomposites was
484 investigated by analyzing the relationship
485 between band gap and varying molar ratios of
486 the components. The photocatalytic
487 degradation efficiency of pollutants is
488 primarily determined by the band gap, which
489 serves as the critical parameter in the process.
490 For this purpose, the absorption spectrum of
491 nanocomposites was measured by a UV-visible
492 device, and the results are shown in Fig. 6(a).
493 The bandgap energies of the samples were
494 determined using Tauc's plots by extrapolating
495 the linear part of plots to the $h\nu$ axis as shown
496 in Fig. 6 (b).

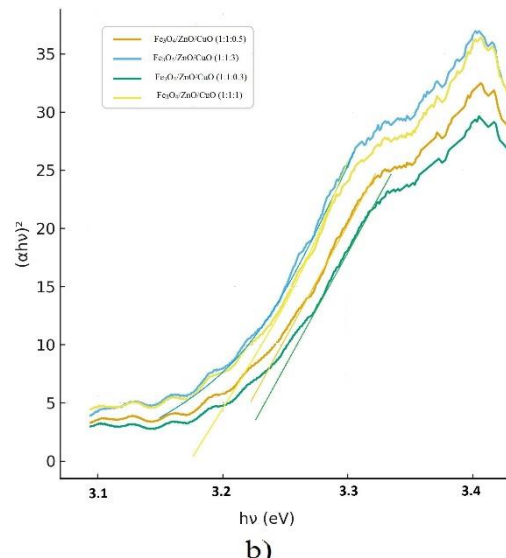
497 ZnO nanoparticles exhibit strong absorption in
498 the wavelength range of 200-400 nm, and the

469 absorption edge of the samples shifts to 372 nm
 470 with increasing copper oxide content in the
 471 visible light region. Coupling zinc oxide with
 472 copper oxide leads to a narrowing of the band
 473 gap. This reduction in the band gap occurs
 474 because the addition of copper oxide to the
 475 nanocomposite introduces an intermediate
 476 energy band at the bottom of the conduction
 477 band of zinc oxide. This interaction decreases
 478 the energy difference between the valence band
 479 and the conduction band of zinc oxide, thereby
 480 reducing the overall band gap energy.
 481 According to the literature, ZnO nanoparticles
 482 are n-type semiconductors, and the
 483 semiconductor CuO nanoparticles are p-type.
 484 In this study, the photocatalytic performance
 485 was enhanced by creating a heterojunction
 486 between n-type and p-type semiconductors,
 487 while simultaneously studying how this
 488 junction influences the optical characteristics.
 489 In Table 3, the absorption wavelength and
 490 energy of the band gap region for each sample
 491 are calculated using the following equation:
 492 $(\alpha h\nu)^2 = A(h\nu - E_g)$ (Eq.4)

493 where α is the absorption coefficient, h is
 494 Planck's constant, ν is the photon frequency,
 495 E_g is the optical band gap, and A and n are
 496 constants. For the direct bandgap
 497 semiconductor, $n = 2$, and for the indirect
 498 transition bandgap, $n = 1/2$. We assumed $n = 2$ for
 499 our samples.



a)



504
 505 **Fig. 6.** Bandgap analysis curves of $\text{Fe}_3\text{O}_4/\text{ZnO}/\text{CuO}$
 506 nanocomposite: a) UV-VIS Absorption Spectra, b)
 507 Tauc's plots graphs ($n=2$)
 508
 509
 510

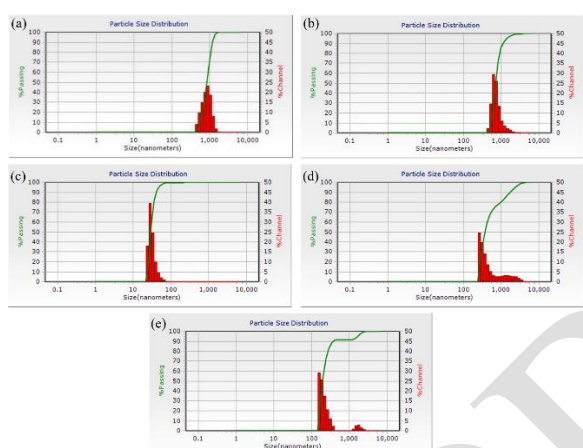
511 **Table 3.** Wavelength values of the absorption edge
 512 and the energy of the band gap of ZnO and
 513 $\text{Fe}_3\text{O}_4/\text{ZnO}/\text{CuO}$ nanocomposites

| Samples | Wavelength of absorption edge (nm) | Energy of the band gap (eV) |
|---|------------------------------------|-----------------------------|
| ZnO | 382.16 | 3.24 |
| $\text{Fe}_3\text{O}_4/\text{ZnO}/\text{CuO}$ (1:1:0.3) | 384.1 | 3.22 |
| $\text{Fe}_3\text{O}_4/\text{ZnO}/\text{CuO}$ (1:1:0.5) | 386.31 | 3.20 |
| $\text{Fe}_3\text{O}_4/\text{ZnO}/\text{CuO}$ (1:1:1) | 389.26 | 3.18 |
| $\text{Fe}_3\text{O}_4/\text{ZnO}/\text{CuO}$ (1:1:3) | 398.54 | 3.11 |

514
 515
 516 DLS analysis was performed to investigate
 517 particle size distribution. Fig. 7 illustrates the
 518 range of particle size distribution in the ZnO,
 519 $\text{Fe}_3\text{O}_4/\text{ZnO}/\text{CuO}$ (1:1:0.3),
 520 $\text{Fe}_3\text{O}_4/\text{ZnO}/\text{CuO}$ (1:1:0.5),
 521 $\text{Fe}_3\text{O}_4/\text{ZnO}/\text{CuO}$ (1:1:1) and
 522 $\text{Fe}_3\text{O}_4/\text{ZnO}/\text{CuO}$ (1:1:3) samples are 486-1944,
 523 486-6540, 25-409, 289-6540, 171.9-6540 nm,
 524 respectively.

525 On the other hand, the highest number of
 526 particles in the ZnO, $\text{Fe}_3\text{O}_4/\text{ZnO}/\text{CuO}$ (1:1:0.3),
 527 $\text{Fe}_3\text{O}_4/\text{ZnO}/\text{CuO}$ (1:1:0.5), $\text{Fe}_3\text{O}_4/\text{ZnO}/\text{CuO}$
 528 (1:1:1), and $\text{Fe}_3\text{O}_4/\text{ZnO}/\text{CuO}$ (1:1:3) samples
 529 are 972, 687, 30.04, 289, and 171.9 nm,
 530 respectively. DLS measures the hydrodynamic
 531 diameter of particles (or agglomerates) in a
 532 solution, which is typically much larger than

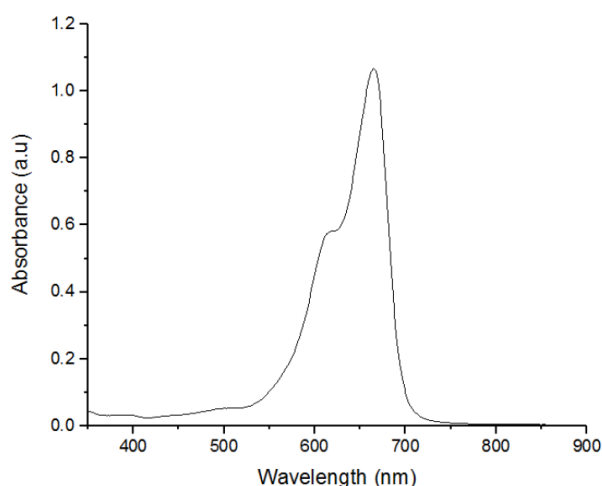
533 the primary particle size seen in SEM or the
 534 crystallite size from XRD. The results show
 535 that increasing the percentages of CuO in the
 536 $\text{Fe}_3\text{O}_4/\text{ZnO}/\text{CuO}$ nanocomposite does not have
 537 a steady effect on particle size. In general,
 538 although the particle size in the nanocomposite
 539 decreased compared to the particle size in pure
 540 ZnO samples but also the DLS data also
 541 indicate severe agglomeration of the primary
 542 nanoparticles in suspension, which is a critical
 543 factor for photocatalytic performance as it
 544 affects the active surface area.
 545



546
 547 **Fig. 7.** DLS Analysis Results of $\text{Fe}_3\text{O}_4/\text{ZnO}/\text{CuO}$
 548 nanocomposites, (a) ZnO , (b) $\text{Fe}_3\text{O}_4/\text{ZnO}/\text{CuO}$
 549 (1:1:0.3),
 550 (c) $\text{Fe}_3\text{O}_4/\text{ZnO}/\text{CuO}$ (1:1:0.5), (d) $\text{Fe}_3\text{O}_4/\text{ZnO}/\text{CuO}$
 551 (1:1:1), (e) $\text{Fe}_3\text{O}_4/\text{ZnO}/\text{CuO}$ (1:1:3)
 552

553 To investigate the various factors that affect the
 554 photocatalytic properties, the $\text{Fe}_3\text{O}_4/\text{ZnO}/\text{CuO}$
 555 nanocomposites with different molar ratios in
 556 MB solution were individually irradiated with
 557 UV and visible waves at 20-40-60-80-100-120
 558 minutes. Fig. 8 shows the absorption spectrum
 559 of MB before photocatalytic activity. The
 560 absorption rate of methylene blue is
 561 approximately 1.067 at 665 nm. The reduction
 562 of this amount in the presence of
 563 $\text{Fe}_3\text{O}_4/\text{ZnO}/\text{CuO}$ nanocomposite and ZnO
 564 samples under visible and UV radiation reflects
 565 the color of this industrial dye. It demonstrates
 566 the ability of this nanocomposite to treat
 567 industrial wastewater.
 568

569

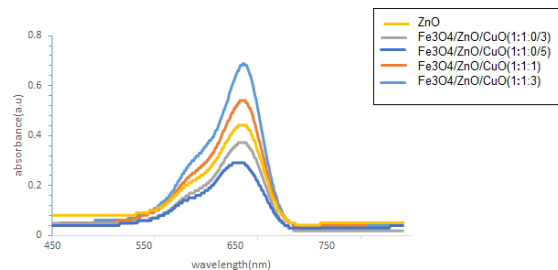


570
 571 **Fig. 8.** Absorption spectrum of methylene blue
 572 before photocatalytic activity.
 573

574 Fig. 9 shows the results of the photocatalytic
 575 activity under UV irradiation for over 120
 576 minutes. The methylene blue absorption peak,
 577 which had an initial concentration of 0.005 g /
 578 L, decreased after 120 min in each sample. The
 579 amount of methylene blue dye removal by the
 580 $\text{Fe}_3\text{O}_4/\text{ZnO}/\text{CuO}$ samples with a molar ratio of
 581 1:1:0.5 is higher than in other samples. The
 582 photocatalytic activity of samples is
 583 58.76%, 65.32%, 72.82%, 49.39%, and 35.33%
 584 for ZnO , $\text{Fe}_3\text{O}_4/\text{ZnO}/\text{CuO}$ with the molar ratio
 585 of 1:1:0.3, 1:1:0.5, 1:1:1, 1:1:3 respectively,
 586 which were calculated using the formula.
 587

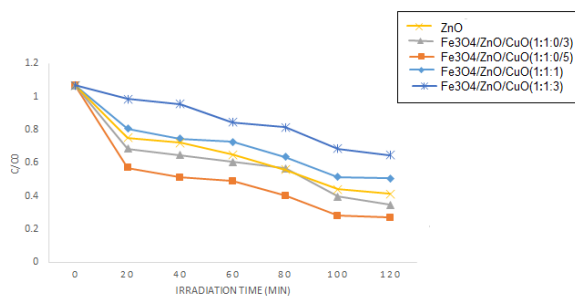
588 Fig. 10 illustrates a comparative diagram of the
 589 photocatalytic performance of $\text{Fe}_3\text{O}_4/\text{ZnO}/\text{CuO}$
 590 nanocomposites with different amounts of CuO
 591 under UV irradiation for 20 to 120 minutes.
 592 Under UV irradiation, $\text{Fe}_3\text{O}_4/\text{ZnO}/\text{CuO}$
 593 nanocomposites with 1:1:1 and 1:1:3 molar
 594 ratios have lower photocatalytic activity than
 595 pure ZnO . The shift of the absorption edge
 596 towards the visible spectrum and the reduction
 597 in band gap of the nanocomposites can be
 598 attributed to the incorporation of CuO. Due to
 599 the differences between the UV wave energy
 600 with the amount of energy which was needed
 601 to transfer electrons from the valence band to
 602 the conduction band in $\text{Fe}_3\text{O}_4/\text{ZnO}/\text{CuO}$
 603 nanocomposites, and the low efficiency of
 604 electron-cavity generation compared to ZnO ,
 605 the above nanocomposites exhibit less
 606 photocatalytic activity.

606



607
608 **Fig. 9.** Photocatalytic activity of $\text{Fe}_3\text{O}_4/\text{ZnO}/\text{CuO}$
609 nanocomposites under UV radiation.

610

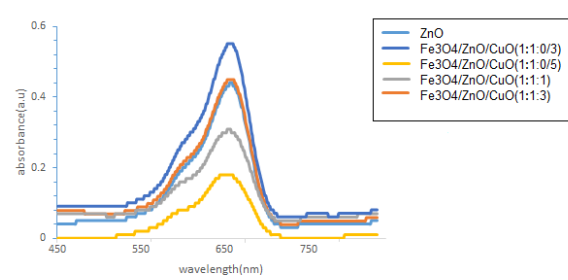


611
612 **Fig. 10.** Comparative diagram of $\text{Fe}_3\text{O}_4/\text{ZnO}/\text{CuO}$
613 nanocomposites' photocatalytic efficiency under
614 UV radiation.

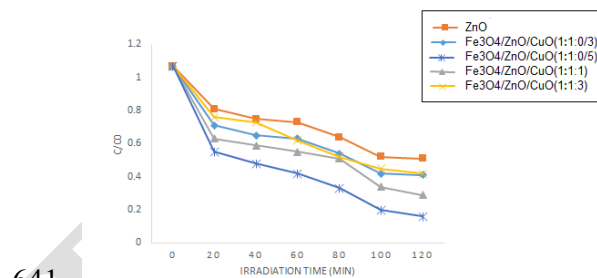
615

616 Fig. 11 shows the results of the photocatalytic
617 activity under visible irradiation for over 120
618 minutes. The $\text{Fe}_3\text{O}_4/\text{ZnO}/\text{CuO}$ composite with
619 a 1:1:0.5 molar ratio demonstrated superior
620 methylene blue dye removal compared to other
621 samples. The photocatalytic degradation
622 efficiencies were measured at 48.45% for pure
623 ZnO , and for $\text{Fe}_3\text{O}_4/\text{ZnO}/\text{CuO}$ composites:
624 62.27% at 1:1:0.3 ratio, 88.7% at 1:1:0.5 ratio,
625 77.94% at 1:1:1 ratio, and 57.82% at 1:1:3
626 ratio. Fig. 12 shows a comparative diagram of
627 the photocatalytic activity of $\text{Fe}_3\text{O}_4/\text{ZnO}/\text{CuO}$
628 nanocomposites with different amounts of CuO
629 under visible irradiation for 20 to 120 minutes.
630 The $\text{Fe}_3\text{O}_4/\text{ZnO}/\text{CuO}$ nanocomposite with a 1:
631 1: 0.5 molar ratio exhibits the best
632 photocatalytic activity. However, the
633 photocatalytic activity of the samples improved
634 concerning pure ZnO , indicating the higher
635 photocatalytic activity of $\text{Fe}_3\text{O}_4/\text{ZnO}/\text{CuO}$
636 nanocomposites in the visible light range.

637

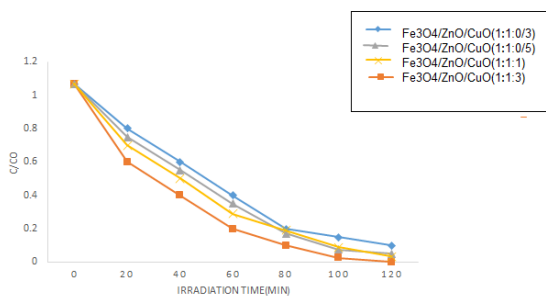


638
639 **Fig. 11.** photocatalytic activity of $\text{Fe}_3\text{O}_4/\text{ZnO}/\text{CuO}$
640 nanocomposites under visible radiation.



641
642 **Fig. 12.** Comparative diagram of photocatalytic
643 efficiency of $\text{Fe}_3\text{O}_4/\text{ZnO}/\text{CuO}$ nanocomposites
644 under visible radiation.

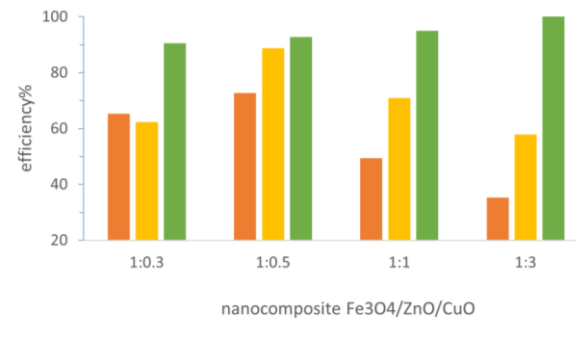
645 To investigate the influence of ultrasound on
646 the photocatalytic activity of the
647 $\text{Fe}_3\text{O}_4/\text{ZnO}/\text{CuO}$ nanocomposites with
648 different molar ratios, the nanocomposites
649 were irradiated with ultrasonic and visible light
650 for 20-120 minutes in a methylene blue
651 solution, and their photocatalytic activity was
652 measured. Fig. 13 illustrates this. The results
653 showed that the $\text{Fe}_3\text{O}_4/\text{ZnO}/\text{CuO}$
654 nanocomposites with the molar ratio of 1:13
655 have the highest photocatalytic activity under
656 ultrasound and visible light irradiation. The
657 enhanced performance can be attributed to
658 CuO 's appropriate band gap characteristics.
659 Under ultrasonic conditions, CuO showed
660 higher activation compared to ZnO , and
661 increasing the CuO content led to improved
662 photocatalytic activity. As illustrated in Fig. 13,
663 complete photocatalytic degradation (100%
664 efficiency) was achieved after 120 minutes of
665 treatment.



667
668 **Fig. 13.** Comparative diagram of photocatalytic
669 efficiency of Fe₃O₄/ZnO/CuO nanocomposites
670 under visible and ultrasound radiation.

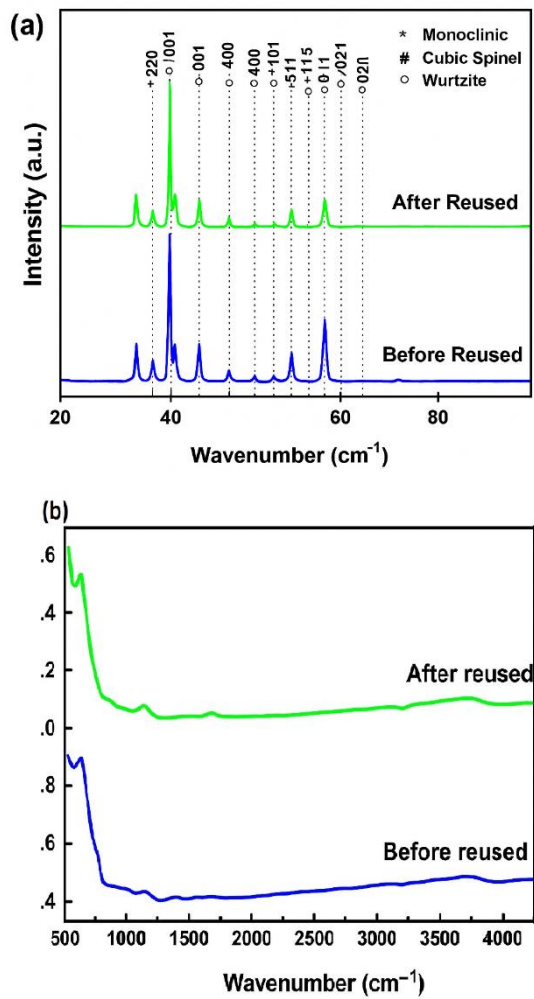
671 The Fe₃O₄/ZnO/CuO nanocomposites with
672 different molar ratios were investigated under
673 UV, visible, and ultrasonic waves, and their
674 comparative results are shown in Fig. 14.
675 Enhancing photocatalytic activity of the
676 nanocomposite under visible light and
677 ultrasonic by increasing CuO content is mainly
678 attributed to the narrow band gap of CuO,
679 which enables strong visible-light absorption
680 and promotes efficient charge separation
681 through the formation of the n-p
682 heterojunction. In this procedure, CuO acts as
683 an effective electron trap, repressing
684 recombination and enhancing the generation of
685 reactive species. Under ultrasonic-visible light,
686 the highest efficiency was observed, which can
687 be driven by two reasons. Firstly, Ultrasonic
688 increases the production of active radicals for
689 photocatalytic activity, and also improves the
690 organic transfer of color between the catalyst
691 surface. secondly, the de-agglomeration of
692 photocatalysis particles by ultrasonication
693 leads to an increase in the specific surface area.
694 The ultrasonic process operates through
695 cavitation that forms holes, leading to elevated

696 temperature and pressure conditions in the
697 reaction medium. This process involves the
698 formation, gradual growth, and eventual
699 bursting of a series of bubbles by sonication.
700 Under such conditions, hot spots are created
701 that can convert water molecules into active
702 hydroxyl radicals and hydrogen peroxide, and
703 these active radicals destroy toxic compounds.



704
705 **Fig. 14.** Comparative diagram of photocatalytic
706 efficiency of Fe₃O₄/ZnO/CuO nanocomposites
707 under UV, visible, and ultrasonic radiation.
708
709

710 Based on other related research, stability of
711 the catalysts under light and ultrasonic
712 irradiation was evaluated by the same batch of
713 nanocomposites for four cycles, with the same
714 amount of fresh MB solutions added after each
715 run. The results in Fig. 15 show that the
716 catalysts exhibit good stability and magnetic
717 recyclability from the treated solutions after
718 successive degradation reactions.
719 The XRD and FTIR measurements were also
720 performed on the catalysts after multiple
721 cycles, and compared with the results obtained
722 before the reaction. In Fig. 15(a), all XRD peaks
723 corresponding to cubic spinel, hexagonal
724 wurtzite, and monoclinic structures remained at
725 the same values after four cycles. So, there is
726 no change in the crystalline structure.
727 The same conclusion is drawn from the IR
728 absorption measurements because the IR peaks
729 of the functional groups remain unchanged
730 after photocatalytic degradation, Fig. 15(b)
731 [30].



732

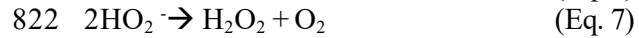
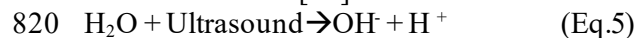
733 **Fig. 15.** a) XRD patterns of $\text{Fe}_3\text{O}_4/\text{ZnO}/\text{CuO}$
 734 nanocomposites after and before reused,b) IR
 735 peaks of $\text{Fe}_3\text{O}_4/\text{ZnO}/\text{CuO}$ nanocomposites after
 736 and before reused [30]

737

738 Various factors such as the generation, trapping
 739 of electrons, charge carrier recombination, the
 740 average size of the crystals, and the energy of
 741 the band gap, are important factors that we can
 742 propose the mechanism of the photocatalyst.
 743 The varying molar proportions of CuO in the
 744 samples significantly influence the
 745 photocatalytic mechanism. Research has
 746 shown that a larger specific surface area creates
 747 more active surface sites, which reduces the
 748 interfacial charge carrier transfer resistance and
 749 enhances photocatalytic performance. The
 750 nanocomposites show different patterns of
 751 photocatalytic performance when exposed to
 752 visible light versus UV radiation.

753 The diffuse reflectance spectroscopy analysis
 754 revealed that ZnO has a band gap of 3.24 eV,
 755 while CuO exhibits a band gap of 1.54 eV[30].
 756 As an n-type semiconductor, ZnO's electrons in
 757 the valence band become excited and move to
 758 the conduction band when exposed to UV
 759 radiation, which is possible due to its specific
 760 band gap energy. In contrast, CuO, being a p-
 761 type semiconductor, can achieve electron
 762 transfer from the valence to the conduction
 763 band through visible light exposure. The
 764 complementary band gap energies of ZnO,
 765 CuO, and Fe_3O_4 can enhance electron transfer
 766 between these materials. When exposed to
 767 visible light, CuO generates electron-hole pairs
 768 because of its favorable band gap.
 769 Additionally, electrons from ZnO's valence
 770 band, which possess lower energy compared to
 771 its conduction band, can move into structural
 772 defects like oxygen vacancies. When CuO's
 773 excited electrons migrate to ZnO's conduction
 774 band, they can interact with Fe^{3+} to form Fe^{2+}
 775 ions. These unstable Fe^{2+} ions then react with
 776 oxygen molecules to generate superoxide
 777 radicals. Simultaneously, holes created in
 778 ZnO's valence band can either transfer to CuO's
 779 valence band or interact with water molecules
 780 to create OH^- . Additionally, holes in CuO can
 781 also generate hydroxyl radicals through water
 782 interaction. Under UV light, the capture of
 783 electrons by Fe^{3+} ions enhances the probability
 784 of hole-mediated hydroxyl radical formation,
 785 which then breaks down organic pollutants.
 786 During this process, electrons from ZnO's
 787 valence band are exclusively excited to its
 788 conduction band, creating holes in the valence
 789 band. These excited electrons are captured by
 790 Fe^{3+} ions, forming Fe^{2+} ions that produce
 791 superoxide radicals. Concurrently, the
 792 photogenerated holes react with water
 793 molecules to form OH^- radicals, which are the
 794 key agents in decomposing methylene blue
 795 during the catalytic reaction [26-28].
 796 The mechanism behind MB degradation using
 797 ultrasonic treatment has been verified. When
 798 ultrasonic waves are applied, they induce
 799 acoustic cavitation, generating extreme
 800 conditions of temperature (5000 K) and
 801 pressure (1000 atm). This process produces
 802 light across a broad wavelength spectrum
 803 (sonoluminescence), activating both ZnO and

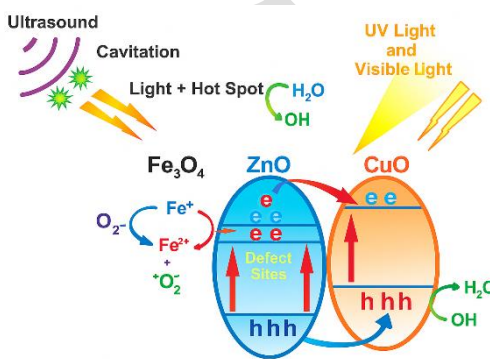
804 CuO semiconductors and forming electron-
 805 hole pairs [28]. These electron-hole pairs
 806 contribute to MB degradation through the same
 807 mechanisms observed in photocatalysis. When
 808 exposed to both visible light and ultrasound,
 809 CuO shows enhanced activation due to its
 810 suitable band gap energy. This explains why
 811 the nanocomposite containing the highest
 812 proportion of CuO ($\text{Fe}_3\text{O}_4/\text{ZnO}/\text{CuO}$ in a 1:1:3
 813 molar ratio) demonstrates superior
 814 photosonocatalytic performance under visible
 815 light conditions. Moreover, the extreme
 816 temperature and pressure conditions created by
 817 ultrasound in aqueous environments promote
 818 the direct formation of OH^- radicals through
 819 Fenton reactions [29]:



824 According to Yuan and colleagues' research
 825 [30], the H_2O_2 produced (as shown in Eq. 7) can
 826 interact with Fe^{2+} to generate OH^- radicals and
 827 Fe^{3+} ions. The increased production of OH^-
 828 radicals through various pathways under
 829 ultrasonic irradiation results in improved
 830 degradation efficiency.

831 The reason that the ternary nanocomposite with
 832 the ratio of 1:1:0.5 is optimal under visible
 833 light, while 1:1:3 is best under sonolysis, is
 834 attributed to the narrow band gap of CuO,
 835 which enables strong visible-light absorption
 836 and promotes efficient charge separation
 837 through the formation of the n-p
 838 heterojunction. In this procedure, CuO acts as
 839 an effective electron trap, repressing
 840 recombination and enhancing the generation of
 841 reactive species. In contrast, under UV
 842 irradiation, increasing the ratio of CuO in the
 843 nanocomposite reduces the photocatalytic
 844 performance because CuO does not absorb UV
 845 efficiently and partially covers the surface of
 846 the primary semiconductor (reducing the

847 specific interface areas). Also, agglomeration
 848 occurs by increasing CuO content, which limits
 849 the UV absorption. Moreover, extra CuO can
 850 behave as recombination centers, accelerating
 851 electron-hole recombination and lowering the
 852 overall photocatalytic activity.



853
 854 **Fig. 16.** Schematic of the photocatalytic
 855 mechanism of $\text{Fe}_3\text{O}_4/\text{ZnO}/\text{CuO}$ nanocomposites

856 **4 Conclusions**

857 In conclusion, the $\text{Fe}_3\text{O}_4/\text{ZnO}/\text{CuO}$
 858 nanocomposites were successfully produced
 859 using the sol-gel synthesis technique. The
 860 degradation of methylene blue was examined
 861 under both light and ultrasonic irradiation to
 862 analyse the photocatalytic activity. Results
 863 revealed that ultrasonic treatment played a
 864 crucial role and significantly improved the
 865 photocatalytic performance of the
 866 nanocomposite materials. The optimal
 867 composition of the photocatalyst
 868 nanocomposite material was investigated
 869 through structural characterization using
 870 various techniques. SEM images shown that
 871 the nanocomposite exhibited a cauliflower-like
 872 structure with particle size distribution ranging
 873 from 25.3 to 57.08 nm, as measured by ImageJ
 874 software. EDX analysis also confirmed
 875 improved dispersion of the samples.
 876 Additionally, dot mapping of the
 877 nanocomposite structure indicated that the
 878 elements were uniformly distributed
 879 throughout the material. Dynamic Light
 880 Scattering (DLS) results showed that
 881 increasing the copper oxide content in the
 882 $\text{Fe}_3\text{O}_4/\text{ZnO}/\text{CuO}$ nanocomposite led to a
 883 reduction in particle size distribution.

884 Moreover, the addition of CuO decreased the
 885 band gap energy, shifting light absorption
 886 toward the visible region. The photocatalytic
 887 performance revealed 100% degradation of
 888 MB for $\text{Fe}_3\text{O}_4/\text{ZnO}/\text{CuO}$ nanocomposite at a
 889 1:1:3 molar ratio under ultrasound and visible
 890 light after 120 minutes. Additionally, the use of
 891 an external magnet allowed for easy separation
 892 and recovery of the nanocomposite from the
 893 solution after the reaction. These findings
 894 highlight the effectiveness of the ternary
 895 $\text{Fe}_3\text{O}_4/\text{ZnO}/\text{CuO}$ nanocomposite catalyst in
 896 removing organic pollutants from wastewater.
 897

Acknowledgements

898 The authors gratefully acknowledge the
 899 mechanical faculty of Tabriz University and
 900 the laboratory of the Materials Science and
 901 Engineering Department of Tabriz University.
 903

904 References

1. Zhu, L.; Zhou, Y.; Fei, L.; Cheng, X.; Zhu, X.; Deng, L.; Ma, X. "Z-scheme $\text{CuO}/\text{Fe}_3\text{O}_4/\text{GO}$ heterojunction photocatalyst: Enhanced photocatalytic performance for elimination of tetracycline." *Chemosphere* 2022, 309 (Pt 2), 136721.
2. Alzuabidi, H. A.; Naghipour, A.; Fardood, S. T. "Green synthesis and characterization of $\text{Cu}_{0.5}\text{Zn}_{0.5}\text{FeAlO}_4$ magnetic nanoparticles with enhanced photocatalytic activity." *J. Ultrafine Grained Nanostruct. Mater.* 2024, 158–167.
3. Hu, Y.; Jensen, L.; Schatz, G. "Photocatalytic reaction pathways on TiO_2 surfaces: a theoretical study." *J. Am. Chem. Soc.* 2006, 128, 15734–42.
4. Ge, M.; Cao, C.; Huang, J.; Li, S.; Chen, Z.; Zhang, K.; et al. "A review of one-dimensional TiO_2 nanostructured materials for environmental and energy
- 929 applications." *Mater. Chem. A* 2016, 4, 6772–6801.
5. Asghar, A.; Aziz, A.; Mohd, A. "Advanced oxidation processes for in situ production of hydrogen peroxide/hydroxyl radical for textile wastewater treatment: a review." *J. Cleaner Prod.* 2015, 87, 826–38.
6. Shakir, A. K.; Ghanbari-Adivi, E.; Baron, A. S.; Soltani, M. "Investigation of the Effect of Calcination Time on the Antibacterial, Antifungal and Anticancer Activities of TiO_2/ZnO Nanocomposites." *Iran. J. Mater. Sci. Eng.* 2025, 22 (1).
7. Safavi, M. S.; Bozorg, S.; Ahadzadeh, I.; Safavi, M. S. "Development of heterogeneous nano-zeolite catalyzing Fenton-like oxidation processes for metalworking fluid wastewater treatment: A comparison with conventional methods." *J. Ultrafine Grained Nanostruct. Mater.* 2024, 190–202.
8. Asai, M. M.; Tapadia, K. "Biofabricated magnetic $\text{CuO}/\text{Fe}_3\text{O}_4$ nanocomposites: Synthesis, characterization and Brilliant Green dye removal from aqueous media and its kinetics study." *J. Indian Chem. Soc.* 2025, 102 (5), 10166.
9. Ajmal, A.; Majeed, I.; Malik, R.; Idriss, H.; Nadeem, M. "Principles and mechanisms of photocatalytic dye degradation on TiO_2 -based photocatalysts: a comparative overview." *RSC Adv.* 2014, 4, 37003–26.
10. Soleimani-Amiri, S.; Hossaini, Z.; Azizi, Z. "Synthesis and investigation of biological activity of new oxazinoazepines: Application of $\text{Fe}_3\text{O}_4/\text{CuO}/\text{ZnO}/\text{MWCNT}$ magnetic nanocomposite in reduction of 4-

973 nitrophenol in water." *Polycycl. 1017*
974 *Aromat. Compd.* 2023, 43 (4), 2938– 1018
975 59.
976 11. Cruz, M.; Gomez, C.; Duran-Valle, C.; 1019
977 Pastrana-Martinez, L.; Faria, J.; Silva, 1020
978 A.; et al. "Bare TiO₂ and graphene 1021
979 oxide TiO₂ photocatalysts on the 1022
980 degradation of selected pesticides and 1023
981 influence of the water matrix." *Appl. 1024
982 Surf. Sci.* 2015, 268, 1–9.
983 12. Rahmat, R.; Heryanto, H.; Ilyas, S.; 1025
984 Fahri, A. N.; Mutmainna, I.; Rahmi, M. 1026
985 H.; Tahir, D. "The relation between 1027
986 structural, optical, and electronic 1028
987 properties of composite CuO/ZnO in 1029
988 supporting photocatalytic 1030
989 performance." *Desalination Water 1031
990 Treat.* 2022, 270, 289–301.
991 13. Shen, Y.; Wang, Y.; Chen, Y.; Park, J. 1032
992 K.; Fang, S.; Feng, K. "Synthesis of 1033
993 Fe₃O₄/CuO/ZnO/RGO and its 1034
994 catalytic degradation of dye 1035
995 wastewater using dielectric barrier 1036
996 discharge plasma." *Arab. J. Chem.* 1037
997 2023, 16 (4), 104571.
998 14. Ohtani, B. "Photocatalysis A to Z – 1038
999 What we know and what we do not 1039
1000 know in a scientific sense." *J. 1040
1001 Photochem. Photobiol. C* 2008, 11, 1041
1002 157–78.
1003 15. Rashid, H.; Muhammad, E.; Hassan, 1042
1004 M.; Rauf, A.; Bashir, A.; Ali, W.; et al. 1043
1005 "Synthesis, structural and 1044
1006 photocatalytic properties of ZnO-CuO, 1045
1007 ZnO-Graphene and ZnO-CuO- 1046
1008 Graphene nanocomposites." 1047
1009 *Polyhedron* 2025, 273, 117471.
1010 16. Li, X.; Liu, J.; Liu, E.; Wan, J.; Bai, Z. 1048
1011 "A review of heterogeneous 1049
1012 photocatalysts for environmental 1050
1013 remediation: materials and processes." 1051
1014 *Chemosphere* 2016, 172, 124–40.
1015 17. Takahashi, M.; Okada, K.; Malfatti, L.; 1052
1016 Innocenzi, P. "Formation of interfaces 1053
1017 responsive and adaptive to 1054
1018 environment via the sol-gel method." 1055
1019 *J. Sol-Gel Sci. Technol.* 2024, 112 (1), 1056
1020 174–81.
1021 18. Malhotra, A.; Saini, A.; Jindal, N.; 1057
1022 Kumar, R. "Combustion synthesized 1058
1023 Fe₃O₄/α-Fe₂O₃/C nanocomposites for 1059
1024 efficient radiative and non-radiative 1059
1025 degradation of methylene blue dye." 1059
1026 *Inorg. Chem. Commun.* 2025, 173, 1059
1027 113808.
1028 19. Bopape, D. A.; Hintsho-Mbita, N. C. 1059
1029 "Commelina benghalensis-mediated 1059
1030 CuO-ZnO nanocomposite: Effect of 1059
1031 the pn heterojunction on the 1059
1032 photocatalytic activity against Congo 1059
1033 red and carbamazepine." *Inorg. Chem. 1059
1034 Commun.* 2025, 154, 114529.
1035 20. Intharaksa, O.; Nanan, S.; 1059
1036 Patdhanagul, N.; Panphojan, T.; 1059
1037 Srikakul, T.; Tantisuwichwong, N.; et 1059
1038 al. "Preparation of magnetic 1059
1039 CuO/Fe₃O₄/ZnO photocatalyst for 1059
1040 complete degradation of methylene 1059
1041 blue under natural sunlight 1059
1042 irradiation." *J. Phys. Chem. Solids* 1059
1043 2023, 182, 111577.
1044 21. Melese, A.; Wubet, W.; Abebe, A.; 1059
1045 Hussen, A. "A comprehensive review 1059
1046 on recent progress in synthesis 1059
1047 methods of ZnO/CuO nanocomposites 1059
1048 and their biological and photocatalytic 1059
1049 applications." *Results Chem.* 2025, 7, 1059
1050 102141.
1051 22. Wahba, M. A.; Yakout, S. M. 1059
1052 "Microwave-synthesized ZrO₂/ZnO 1059
1053 heterostructures: fast and high charge 1059
1054 separation solar catalysts for dyes- 1059
1055 waste degradation." *J. Sol-Gel Sci. 1059
1056 Technol.* 2022, 104 (2), 330–41.
1057 23. Ross, J. R. H. "Catalyst 1059
1058 characterization." In *Contemporary 1059
1059 Catalysts Fundamentals and Current 1059*

1060 *Applications*; 2019; Chapter 5, pp 121–
1061 132.

1062 24. Chen, X.; Selloni, A. "Introduction:
1063 Titanium dioxide (TiO_2)
1064 nanomaterials." *Chem. Rev.* 2014, **114**,
1065 9281–82.

1066 25. Etay, H.; Kumar, A.; Yadav, O. P.
1067 "Kinetics of photocatalytic
1068 degradation of methylene blue dye in
1069 aqueous medium using ZnO
1070 nanoparticles under UV radiation." *J.
1071 Anal. Pharm. Res.* 2023, **12** (1).

1072 26. Asli, S. A.; Taghizadeh, M.
1073 "Sonophotocatalytic degradation of
1074 pollutants by ZnO -based catalysts: A
1075 review." *Chem. Select* 2020, 13720–
1076 73.

1077 27. Benamara, M.; Nassar, K. I.; Essid, M.;
1078 Frick, S.; Rugmini, R.; Sekhar, K. C.;
1079 Silva, J. P. "Visible light-driven
1080 removal of Rhodamine B using
1081 indium-doped zinc oxide prepared by
1082 sol–gel method." *J. Sol-Gel Sci.
1083 Technol.* 2024, **111** (2), 553–65.

1084 28. Yuan, N.; Zhang, G.; Guo, S.; Wan, Z.
1085 "Enhanced ultrasound-assisted
1086 degradation of methyl orange and
1087 metronidazole by rectorite-supported
1088 nanoscale zero-valent iron." *Ultrason.
1089 Sonochem.* 2016, **28**, 62.

1090 29. Khan, M. A. N.; Siddique, M.; Wahid,
1091 F.; Khan, R. "Removal of reactive blue
1092 19 dye by sono, photo and
1093 sonophotocatalytic oxidation using
1094 visible light." *Ultrason. Sonochem.*
1095 2015, **26**, 370–77.

1096 30. Taufik, A.; Saleh, R. "Synthesis of iron
1097 (II, III) oxide/zinc oxide/copper (II)
1098 oxide($Fe_3O_4/ZnO/CuO$)
1099 nanocomposites and their
1100 photosonocatalytic property for
1101 organic dye removal." *J. Colloid
1102 Interface Sci.* 2017, **491**, 27–36.